First results from PHENIX experiment at RHIC

V.S. Pantuev for the PHENIX collaboration

Dep. of Physics and Astronomy, State University of New York at Stony Brook, Stony Brook, New York, 11794-3800, USA

Abstract. The PHENIX experiment has successfully measured nuclear reactions of Au + Au at $\sqrt{s_{NN}} = 130$ GeV. First results on particle multiplicities, mean trasnsverse energy, charged particles and identified hadrons spectra, elliptic flow, and high momentum particles are presented.

INTRODUCTION

Ultrarelativistic heavy-ion collisions provide the unique opprtunity to study the properties of strongly interacting matter under extreme conditions. With the beginning of the Relativistic Heavy Ion Collider (RHIC) operation, a new regime of availible c.m. energy $\sqrt{s_{NN}}$ opened up for experimental exploration. The initial temperature and density reached in heavy ion collisions at RHIC are expected to be sufficiently high to invoke the phase transition of normal nuclear matter into a phase of deconfined quarks and gluons, known as the Quark Gluon Plasma (QGP). At the same time, the restoration of chiral symmetry is expected under these conditions.

The PHENIX experiment, one of the four experiments at RHIC, is designed to measure a variaty of particles. In particular to investigate penetrating probes, like photons, electrons and muons. These probes could bring information about the initial stage of the collisions since they reflect processes like dilepton decays of vector mesons including J/ψ's, semi-lepton decays of particles carrying open charm or bottom, and thermal radiation. At the same time, the PHENIX experiment provides the capabilities to detect the obvervables sensitive to all stages of the collision. Among these probes are charged particled and identified hadrons which provide insight into the dynamical evolution of the system and allow to characterize the conditions at freeze-out. At the first year running of the PHENIX accumulated the significant statistics for global observables, like particle multiplisity and transverse energy, charged particle spectra and neutral pions.

THE PHENIX DETECTOR

The baseline detector systems in PHENIX are shown in Fig. 1. PHENIX [1] has four spectrometer arms: two Central Arms, each covering 90^o in azimuth for pseudorapidity $|\eta| < 0.35$ and two Muon Arms at $1.1 < |\eta| < 2.4$. There are three magnets: the Central Magnet provides an axial magnetic field for the Central Arms while the Muon Magnets produce radial fields for the Muon Arms.

In general, the detectors can be grouped as follows:

1. Vertex and Trigger detectors: Zero-Degree Calorimeters (ZDC), Beam-Beam Counters (BBC), Multiplicity/Vertex Detector (MVD). These detectors are positioned along the collision axis.
2. Central Arm Detectors. These detectors are all positioned radially about the collision axis, exending from 2 m to 5 m.
   (a) Charged Tracking system: Drift Chambers (DC), Pad Chambers (PC), Time Expansion Chambers (TEC). There are two DCs, three PCs, and one TEC positioned radially from the collision axis about midrapidity.
   (b) Ring Imaging Cherenkov Detector (RICH). There are two RICH.
   (c) Time-of-Flight System (TOF). The TOF is positioned in one arm only (the East) and has half the acceptance in azimuth as the Drift Chambers.

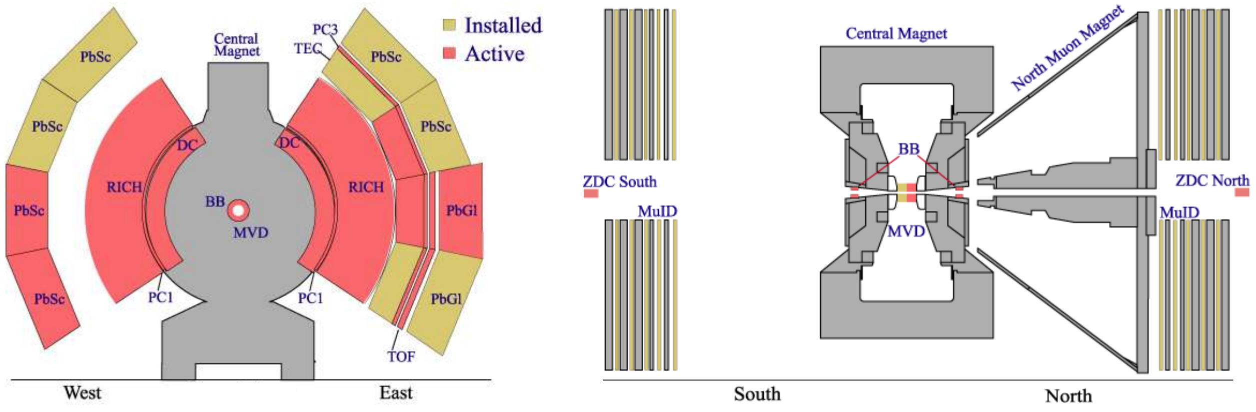

FIGURE 1. The experimental setup in PHENIX for the central arm spectrometer. The top picture is the cross-sectional view of PHENIX transverse to the beam axis while the bottom shows the beam-axis subsystems.

   (d) Electromagnetic Calorimetry (PbGl and PbSc).

3. Muon Arms with tracking and particle identification chambers. These spectrometers were not used in Year-2000 runs.

Vertex and Trigger Detectors

There are dedicated subsystems that determine the vertex of each collision in PHENIX. These include the Zero Degree Calorimeters, the Beam-beam Counters and the Multiplicity Vertex Detector (the collison axis detectors as shown schematically in Fig. 1).

The ZDCs are RHIC standard detectors that measure the fraction of the energy deposited by spectator neutrons during the collisions and serve as an event trigger for each RHIC experiment. In PHENIX, two ZDCs are positioned North and South close to the Muon Spectrometers along the beam axis subtending the polar angle $|\theta| < 4$ mrad. Using the measured time difference between BBC the vertex position of the event along the collision axis is determined. For the Summer 2000 runs, the total number of 5M events were recorded at $\sqrt{s_{NN}} = 130$ GeV.

There are two Beam-Beam counters each positioned 1.4 meters from the interaction point just behind the central magnet poles along the beam axis. Each Counter consists of 64 Cherekov telescopes, arranged radially about the collision axis and situated north and south of the Multiplicity Vertex Detector. The BBCs measure the fast particles produced in each collision at these forward angles. Using the measured time difference between BBC the vertex position of the event along the collision axis is determined. For the Summer 2000 runs, the total number of 5M events were recorded at $\sqrt{s_{NN}} = 130$ GeV.

The MVD is composed of concentric barrels of silicon strip detectors and end-caps of silican pad detectors. It measures the multiplicity of charged particles produced close to the beam axis in each event. The MVD was not used in year 2000.

Central Arm Spectrometers

The central arm spectrometers use a central magnet that produces an approximately axially symmetric field that focusses the tracks into the detector acceptance. The Central Magnet (CM) weighs about 500 tons and provides a total field integral of 0.78 T·m at 90 degrees in polar angle from the beam axis. This results in a single particle momentum resolution of $0.6\% + 3.5\% * p$ where "p" is momentum in $[GeV/c]$ as measured in the Drift Chambers.

The drift chambers are the first tracking detectors charged particles encounter as they traverse through the central arms. Each subtends 90^o in azimuth about the beam axis and measures the track curvature between 2.02 and 2.46 meters radially, from which the momentum is determined. The chambers extend in length to a total of 1.8 meters along the beam axis. The interior of each DC is composed of 40 planes of wires along the radius, containing X- and UV-stereo sections. These sections are arranged into 160 drift cells in azimuth angle.

Each Pad Chamber in PHENIX measures a three-dimensional space point of a charged track to within a few millimeters. The pad chamber detectors are used in the global track reconstruction to determine the polar angle of the track and to minimize the background contribution of albedo and non-vertex decay particles. The Pad Chambers are also used in the no-field runs to determine the total charged particle multiplicity distribution. In Year-2000, three Pad Chambers were positioned in PHENIX. Two were located in the East Arm: PC1 is mounted behind Drift Chamber and PC3 was positioned directly behind the Time Expansion Chamber and in front of the Time-of-Flight Hodoscope. In the West Arm PC1 was mounted behind Drift Chamber.

The Time Expansion Chamber (TEC) is located in the East arm. It is designed primarily for e/π separation and tracking in front of the EM Calorimeter. The TEC also has particle identification capabilities using energy loss (dE/dx) and momentum reconstruction for high transverse momentum particles.

The Time-of-Flight (TOF) hodoscope subtends 45^o in azimuth in the East arm (see Fig. 1).TOF detector is finely segmented to accountfor the high detector occupancy in Au+Au collision. The TOF have a total of 960 plastic scintillation counters (BC 404) and 1920 channels of Photomultiplier tubes (PTM). Each slat has a light guide, support and PMTs at either end. In Year-2000, the measured TOF resolution was 115 ps.

The Ring Imaging Cherenkov (RICH) detector subsystem serves as one of the primary detectors for the identification of electrons. Each of two detectors consists of radiator gas vessel appoximately 1.5-m deep in track direction, 6-m wide in beam direction and spans 90^o in ϕ. In addition it has 48 focusing mirrows with fine tuning and focal plane with 2560 UV-sensitive Photomultiplier tubes.

The Electromagnetic Calorimeters in PHENIX measure photons and dileptons. There are a total of 8 sectors (4 in each arm) of two types of Electromagnetic Calorimeters in PHENIX: 6 sectors of lead scintillator (PbSc or “shashlik”) with 20,000 readout channels and 2 sectors of lead glass (PbGl) with 10,000 channels. The calorimeters are positioned in the outer layers of PHENIX $\approx$ 5 meters radially from the collision axis and cover appoximately 60 m^2.

The perfomance of PHENIX detector subsystems in Year-2000 are presented in Table 1.

TABLE 1. Resolution and positions in r, ϕ, and η of PHENIX subsystems. Detectors not used in Year-2000 have a line.

Detector	Year-2000 Resolution	$\Delta\phi$ (rad)	η
ZDC	$\sigma_E/E < 20\%$ at $E_n = 100GeV$	10.0cm square	$6.0 < \lvert\eta\rvert$
BBC	$\sigma_z = 1.5$cm, $\sigma_t = 70$ps	2π	$3.0 < \lvert\eta\rvert < 3.9$
MVD	—	2π	$\lvert\eta\rvert < 0.43$
DC	160μm	$\pi/2$	$\lvert\eta\rvert < 0.35$
PC I	$\sigma_y = 1.62$mm $\sigma_z = 2.3$mm	$\pi/2$	$\lvert\eta\rvert < 0.35$
PC II	—	$\pi/2$	$\lvert\eta\rvert < 0.35$
PC III	$\sigma_y = 3.2$mm $\sigma_z = 4.8$mm	$\pi/2$	$\lvert\eta\rvert < 0.35$
TEC	380μm	$\pi/2$	$\lvert\eta\rvert < 0.35$
TOF	115 ps	$\pi/4$	$\lvert\eta\rvert < 0.35$
RICH		$\pi/2$	$\lvert\eta\rvert < 0.35$
PbGl	$\sigma_E/\sqrt{E}(\%) = 5.8\%/\sqrt{E(GeV)} \bigoplus 1.0$ $\sigma_t(ps) = 70/\sqrt{E(GeV)} \bigoplus 70$	$\pi/4$	$\lvert\eta\rvert < 0.38$
PbSc	$8\%/\sqrt{E(GeV)} \bigoplus 1.9\%$ $\sigma_t(ps) = 143/\sqrt{E(GeV)} \bigoplus 75$	$\pi/4$	$\lvert\eta\rvert < 0.38$
μ Spect	—		$1.1 < \lvert\eta\rvert < 2.4$

EVENT CENTRALITY SELECTION

For the first physics run coincidences between the BBC counters and ZDC calorimeters were used as independent minimum bias triggers. At least two photomultiplier fires has been requared in each BBC. A total of about 5 million events for Au+Au collisions was recorded.

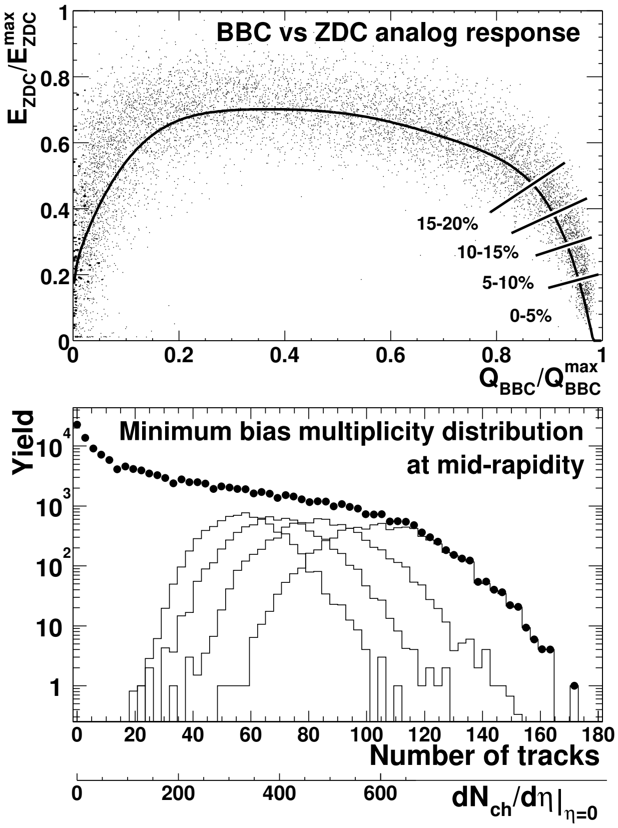

FIGURE 2. BBC vs. ZDC analog response (top panel) and minimum-bias multiplicity distribution in the PHENIX measurement aperture (lower panel). The lower axis converts the observed distribution to the corresponding average $dN_{ch}/d\eta$ for track multiplicities less than $\sim$ 120; beyond that value the shape of the distribution has a significant contribution from fluctuations into the measurement aperture.

Based on detailed simulations of the BBC, this trigger reflects $[92 \pm 2(syst)]\%$ of the nuclear interaction cross section of 7.2 barns [2]. Another trigger is generated by a coincidence between the two ZDC, each one with an energy signal larger than 10 GeV. This trigger reflects the nuclear interaction plus the mutual Coulomb dissociation cross sections. Most BBC triggers (97.8%) also satisfy the ZDC trigger requirement. The small percentage of exclusive BBC triggers is due to inefficiencies of the ZDC trigger and background interactions. To exclude upstream and downstream beam-gas interactions and a possible background of particles scattered from the magnetic poles the collision vertex position cut $|z| < 20$ cm was applied.

To select $Au+Au$ collisions versus its centrality an information from both ZDC and BBC has been used as shown on top panel of Fig. 2. In order to avoid the ambiguities inherent in the BBC vs. ZDC distribution, we selected events with increasing centrality based upon the monotonic response of another PHENIX detector. The centroids of these events projected onto the ZDC-BBC space determine the centrality contour indicated by the solid line. The cuts are made perpendicular to this contour. Simulations of the BBC and ZDC response were used to account for the effect of physics and detector fluctuations in the definition of these event classes and to relate them via a Glauber model [2] to the number of participating nucleons N_p and of binary collisions N_c, Table 2.

CENTRALITY DEPENDENCE OF CHARGED PARTICLE MULTIPLISITY

Particle density at midrapidity is an essential global variable for the characterization of high energy nuclear collisions, providing information about the initial conditions, such as energy density. The results presented here should help to constrain the wide range of theoretical predictions [3] available at RHIC energies and to discriminate among various

TABLE 2. Charged-particle density, number of participants and collisions for various centrality bins expressed as percentiles of σ_{geo}=7.2 b. The statistical errors are negligible and only systematic errors are quoted.

Centrality bin	$< dN_{ch}/d\eta_{\vert\eta=0} >$	$< N_p >$	$< N_c >$
0 - 5	622 ± 41	347 ± 10	946 ± 146
5 - 10	498 ± 31	293 ± 9	749 ± 116
10 - 15	413 ± 25	248 ± 8	596 ± 93
15 - 20	344 ± 21	211 ± 7	478 ± 75
20 - 25	287 ± 18	177 ± 7	377 ± 61
25 - 30	235 ± 16	146 ± 6	290 ± 47
30 - 35	188 ± 14	122 ± 5	226 ± 38
35 - 40	147 ± 12	99 ± 5	170 ± 30
40 - 45	115 ± 11	82 ± 5	130 ± 24
45 - 50	89 ± 9	68 ± 4	101 ± 19

mechanisms of entropy and particle production. In particular, we analyze the particle density as a function of centrality, expressed by the number of participating nucleons. Such an analysis may shed light on the relative importance of soft versus hard processes of particle production and test the assumption of gluon saturation expected at RHIC energies [4, 5]. Our results are compared to different models, to similar studies obtained in Pb-Pb collisions at the CERN SPS [6, 7, 8] and to a recent measurement performed at RHIC by PHOBOS [9].

This analysis is based on a sample of 140,000 events taken without magnetic field, satisfying the BBC trigger and with a reconstructed vertex position [10]. The number of primary charged particles per event is determined on a statistical basis by correlating hits in PC1 and PC3. The vertex is reconstructed using the following algorithm: all hits in PC3 are combined with all hits in PC1 and the resulting lines are projected onto a plane through the beam line, perpendicular to the symmetry axis of the chambers. Once the vertex is known, all hits in PC3 are again combined with all hits in PC1 and the resulting tracks are projected onto the plane previously defined. Combinatorial background inherent to the adopted procedure of combining all hits in PC3 with all hits in PC1. This background was determined by a mixed event technique: each sector in PC1 was exchanged with its neighbor. After subtracting the background, and applying the appropriate corretions [10] we obtain the minimum-bias charged particle multiplicity distribution, Fig. 2. This figure also shows the multimpicity distribution for the four most central bins, $0\% - 5\%$ to $15\% - 20\%$. The average charged particle density scaled up to one unit of rapidity and the corresponding numbers N_p and N_c are tabulated in Table 2 for various centrality bins.

Models such as HIJING predict that there is a component of particle production from soft interactions that scales linearly with N_p and a second component from hard processes (pQCD jets) that scales with N_c. Following that, we fit the data of Figure 3 with the function $dN_{ch}/d\eta = A \times N_p + B \times N_c$ using the values of N_c and N_p tabulated in Table 2. The results of the fit are shown in Fig. 3. In such models, the values of A and B imply a large contribution of hard process to particle production, which increases with centrality from $\sim 30\%$ at N_p=68 to $\sim 50\%$ for central collisions. HIJING predicts the same trend although the calculated values are lower than the data by $\sim 15\%$.

Other models such as the EKRT [5] predict that at RHIC energies, the large production of semi-hard gluons in a small volume may saturate the gluon density. The resulting gluon fusion limits the total entropy production and thus lowers the final particle production per participant. The predictions of the EKRT model are also shown in Fig. 3. We observe no such saturation effect but instead see a steady rise in the particle production per participant pair.

TRANSVERSE ENERGY DISTRIBUTION

The transition to a quark-gluon plasma had been predicted to occur at energy density on the order of a few GeV/fm^3. The spatial energy density (ε) in a relativistic collision can be estimated (following Bjorken [12]) by measuring the transverse energy density in rapidity, dE_T/dy. In PHENIX the electromagnetic calorimeter in central spectrometer has been used to estimate transverse enegry in the collisioin [11]. The performance of calorimeter is illustrated in Fig. 4.

Following a procedure used in the previous sectioin, we calculate $\langle dE_T/d\eta|_{\eta=0}\rangle = 578^{+26}_{-39}$ GeV for most 0-2% central events. It gives $\varepsilon_{Bj} = 4.6$ GeV/fm^3 or an increase of 60% compared to CERN energy [13]. Fig. 5a shows that $\langle dE_T/d\eta|_{\eta=0}\rangle$ per participant also increases with N_{part}, closely paralleling the rise in charged particle density and the ratio $\langle dE_T/d\eta|_{\eta=0}\rangle/\langle dN_{ch}/d\eta|_{\eta=0}\rangle$ remains constant at a value of ~ 0.8 GeV, independent of centrality. This

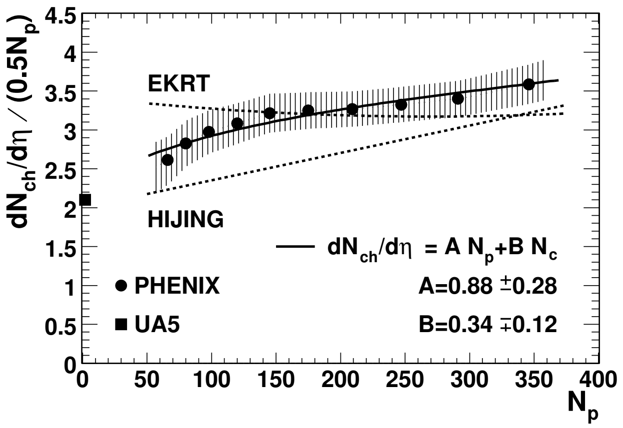

FIGURE 3. Charged-particle pseudorapidity density per participant pair vs. the number of participants. Predictions from HIJING [4] and EKRT [5] models, and a simple phenomenological fit are also shown. The shaded area represents the systematic errors of $dN_{ch}/d\eta$ and N_p. The errors of N_c are in Table 2.

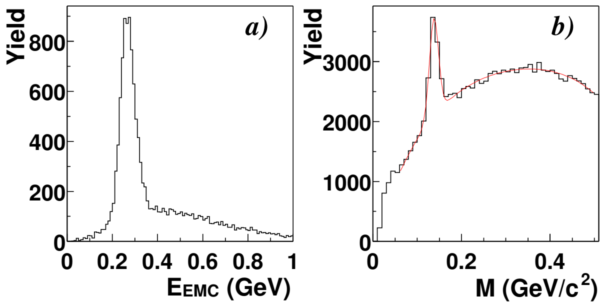

FIGURE 4. (a) The distribution of EMCal clusters corresponding to 1 GeV/c charged tracks (mostly pions) from Au+Au collisions. (b) The reconstructed π^0 mass from pairs of EMCal clusters with total energy > 2 GeV.

indicates that the additional energy density at RHIC energies is achieved mainly by an increase in particle production rather than by an increase in transverse energy per particle.

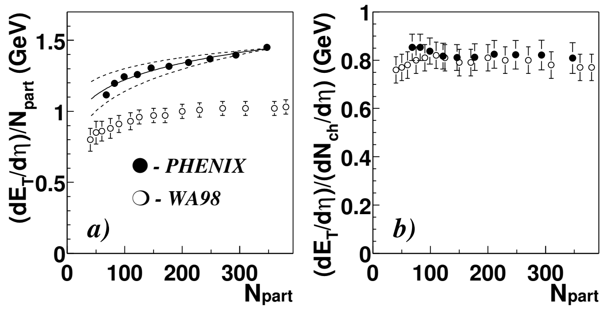

FIGURE 5. (a) PHENIX transverse energy density per participant $dE_T/d\eta|_{\eta=0}/N_{\rm part}$ for Au+Au collisions at $\sqrt{s_{NN}} = 130$ GeV as a function of $N_{\rm part}$, the number of participants, compared to data from WA98 cite:wa98 for Pb+Pb collisions at $\sqrt{s_{NN}} = 17.2$ GeV. The solid line is the $N_{\rm part}^{\alpha}$ best fit and the dashed lines represent the effect of the $\pm 1\sigma$ $N_{\rm part}$-dependent systematic errors for $dE_T/d\eta|_{\eta=0}$ and $N_{\rm part}$. (b) PHENIX $dE_T/d\eta|_{\eta=0}/dN_{ch}/d\eta|_{\eta=0}$ versus $N_{\rm part}$, including all systematic errors, compared to WA98.

ELLIPTIC FLOW

Elliptic flow is one of the probes which allow to study properties of high-energy-density nuclear matter. Over a broad range of beam energies, elliptic flow can be attributed to a delicate balance between (i) the ability of a fast pressure build-up to generate a rapid transverse expansion of nuclear matter and (ii) the passage time for removal of the shadowing effect on participant hadrons by the projectile and target spectators. If the passage time is long compared to the expansion time, spectator nucleons serve to block the path of participant hadrons emitted toward the reaction plane, and nuclear matter is squeezed-out perpendicular to this plane giving rise to negative elliptic flow. Thus, elliptic flow is predicted and found to be negative for beam energies < 4 AGeV and positive for beam energies > 4 AGeV [15, 16, 17]. For RHIC energies, strong Lorentz contraction and very short passage times lead to significant reduction of shadowing effects, and positive elliptic flow is expected [14, 18, 19].

In PHENIX, two-particle azimuthal correlation measurements are exploited to evaluate the elliptic flow of charged hadrons. Data analysis is based on the use of the second Fourier coefficient, $\lambda_2 = \langle \cos(2\Delta\phi) \rangle$, to measure the anisotropy of the distribution in the azimuthal angle difference ($\Delta\phi = \phi_1 - \phi_2$) between pairs of charged hadrons [20]:

$$\frac{dN}{d(\Delta\phi)} \propto [1 + 2\lambda_1 \cos(\Delta\phi) + 2\lambda_2 \cos(2\Delta\phi)]\,. \tag{1}$$

A two-particle azimuthal correlation function can be defined as [20, 21]

$$C(\Delta\phi) = \frac{N_{cor}(\Delta\phi)}{N_{uncor}(\Delta\phi)}, \tag{2}$$

where $N_{cor}(\Delta\phi)$ is the observed $\Delta\phi$ distribution for charged particle or track pairs selected from the same event, and $N_{uncor}(\Delta\phi)$ is the $\Delta\phi$ distribution for particle pairs selected from mixed events.

Fig. 6a and b show representative distributions for particle pairs obtained from the same event ($N_{cor}(\Delta\phi)$) and those obtained from mixed events ($N_{uncor}(\Delta\phi)$) respectively. The correlation function $C(\Delta\phi)$, obtained from the ratio of these two distributions (cf Eq. 2) is shown in Fig. 6c. The correlation function shows a clear anisotropic pattern which is essentially symmetric about $\Delta\phi = 90^o$.

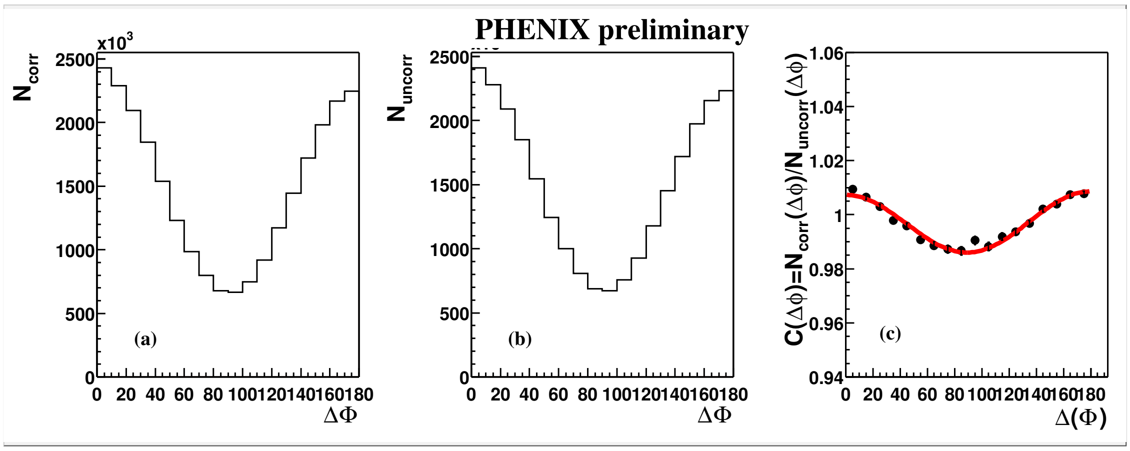

FIGURE 6. $\Delta\phi$ distributions for charged particle or track pairs selected from the same event (a) and for particle pairs selected from mixed events (b). The resulting correlation function $C(\Delta\phi)$, obtained from the ratio of these two distributions is shown in panel (c).

The magnitude of the elliptic flow usually expressed via the Fourier coefficient $\sqrt{\lambda_2} = v_2$. The dependence of this coefficient on particle transverse momentum and centraly is presented in Figure 7. The measurements indicate large flow magnitudes. The differential flow $v_2(p_t)$ and $v_2(cent)$ is increasing with transverse momentum of emitted hadron and with for larger inpact parameter.

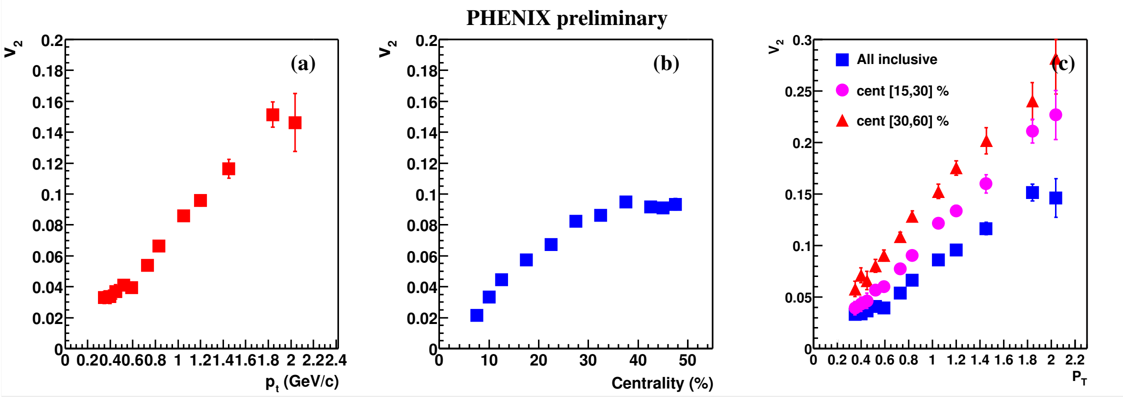

FIGURE 7. v_2 vs. p_t (a), v_2 vs. centrality (b), and v_2 vs. p_t for several different centralities (inclusive, 15-30%, and 30 - 60%) as indicated. Error bars indicate statistical errors only.

IDENTIFIED CHARGED HADRON SPECTRA

Identified hadron spectroscopy provides a tool for studing the reaction dynamics beyond that of global even charcterization. Their yields provide information about the initial particle production, while the spectral shapes reflect the dynamical evolution of the system. More specifically, the mass and centrality dependence of the spectra can help to identify collective motion as predicted in hydrodynamical descriptions [22, 23] or other modification by the surrounding partonic and hadronic medium [24, 25]. Yields of mesons and baryons indicate the rate of strange and anti-quark production; nuclear effects should modify the yield per participating nucleon compared to that in p+p collisions.
Her we present first results on identified pion, kaon, proton, and anti-proton production as a function of collision centrality.

PHENIX tracking and Time-of-Flight systems were used to identify charged hadros by its momemtum and velocity. Fig. 8 shows the p_t spectra for π^+, K^+, p (left panel) and $\pi^-, K^-, \overline{p}$ (right panel) for the most central, mid-central and peripheral collisions.

The systematic uncertainties are of $\approx 11\%$ for all particles species. Going from peripheral (bottom panels) to central events (top panels) we observe that the pion spectra change from a concave shape which is well described by power-law parametrization [38] to almost exponential in p_t for the most central selection. The inverse transverse mass slopes increase with particle mass and with centrality. This behavior has been previously observed in lower energy heavy ion collisions at CERN-SPS [26, 27] and at BNL-AGS [28] and was attributed to collective radial motion (flow) in the rapidly expanding system.

A new feature observed for the first time at RHIC is that at $p_t \approx 2$ GeV/c the hadron yields are dominated by protons and anti-protons. In central events the proton spectra cross the π^+ spectra at $p_t = 1.6$ GeV/c, while the $\pi^-/\overline{p}$ crossing occurs at $p_t \approx 2$GeV/c. In peripheral events the π^+ spectra are above the proton spectra in the entire measured p_t range. Negatively charged particles behave in a similar way, although due to the smaller yield of anti-protons, compared to protons, the $\pi^-/\overline{p}$ crossing is only observed for the two most central event classes.

It is feasible that hydro-dynamic expansion alone or combined with hadronic re-scattering is responsible for the baryon dominance at high p_t [22, 23, 29]. Protons/anti-protons produced via a baryon junction mechanism combined with jet-quenching in the pion channel are shown to exhibit the same effect [30]. Intrinsic p_t broadening caused by gluon saturation expected in high-density QCD [24, 25] gives an alternative explanation. Interplay between longitudinal Bjorken expansion (red shift) and transverse flow (blue shift) [31] has also been shown to agree with the data.

Fig.9 shows the mean p_t as a function of N_{part} for π^+, K^+, p (left panel) and $\pi^-, K^-, \overline{p}$ (right panel). The full points are the PHENIX measurement, while the open points at $N_{part} = 2$ are interpolations to $\sqrt{s} = 130$ GeV obtained from pp and $p\overline{p}$ data at lower and higher energies[32],respectively. In peripheral Au-Au collisions at RHIC pions and kaons is exhibit similar $\langle p_t \rangle$ to those in pp collisions, but protons and anti-protons have significantly higher $\langle p_t \rangle$, indicating that nuclear effects are important even at small N_{part}.

The hadron yields per participant as a function of N_{part} are shown in Fig. 10.

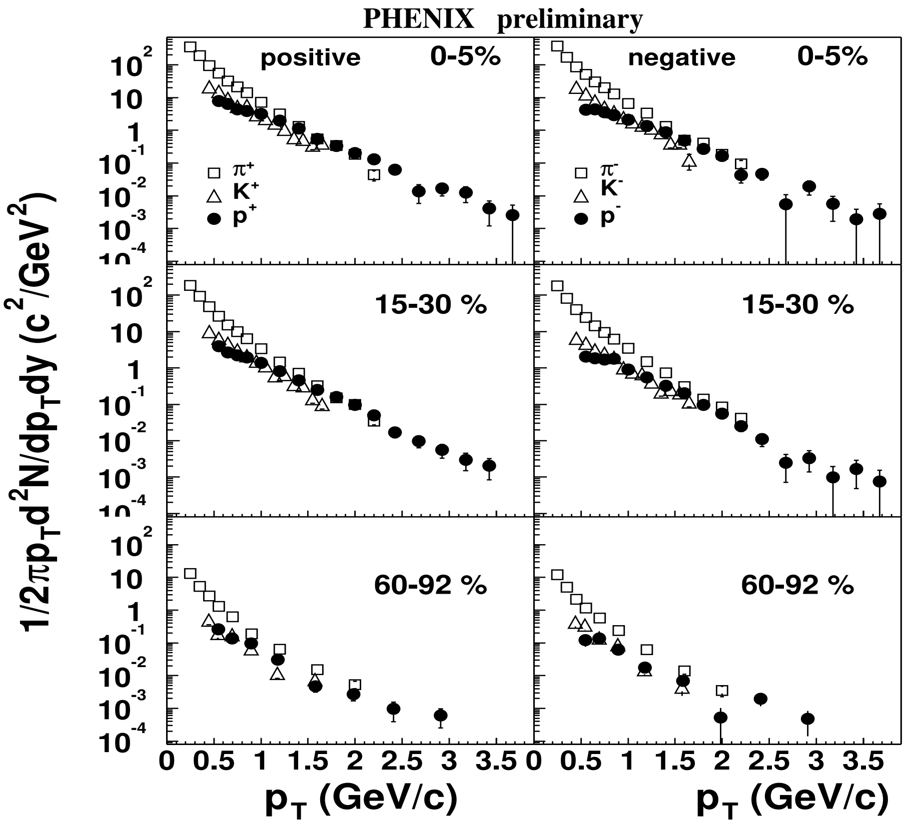

FIGURE 8. Transverse momentum spectra measured at mid-rapidity normalized to $|y| < 0.5$ for π^+, K^+, p (left) and $\pi^-, K^-, \overline{p}$ (right) at three different event centralities. The centrality selections are indicated in each panel. The symbols indicated in the top panels apply for all centrality selections.

SUPPRESSION OF HADRONS WITH LARGE TRANSVERSE MOMENTUM IN CENTRAL COLLISIONS

In AA collisions of particular interest are the products of parton scatterings with large momentum transfer ("hard scatterings"). In p+p collisions hard-scattered partons fragment into jets of hadrons and manifest themselves as a primary source of hadrons at high transverse momentum (p_T), typically above $\sim$2 GeV/c. In a high-energy nuclear collision hard scattering will occur at the earliest time during the collision, well before the QGP is expected to form, and thus the scattered partons will subsequently experience the strongly interacting medium created in the collision. These partons are expected to lose energy [33] in hot and dense nuclear matter through gluon bremsstrahlung, effectively quenching jet production. This would have many observable consequences, of which the most directly measurable would be a depletion in the yield of high p_T hadrons [40]. It has been suggested that the energy loss is larger in a medium of deconfined color charges than in hadronic matter [34], making "jet quenching" a potential signature for QGP formation. Given that hard parton scatterings have small cross sections, one can regard the nuclei as an incoherent superposition of partons ("point-like scaling"). We approximate this by modelling the A+A collision as a sum of independent nucleon-nucleon (N+N) collisions ("binary scaling"). For a given class of A+A collisions, we can determine $\langle N_{binary} \rangle$ (see Table 2) the average number of inelastic N+N collisions per event and then define the *nuclear*

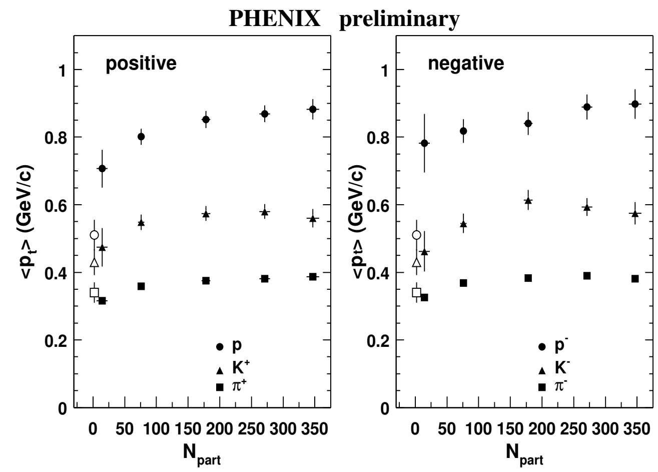

FIGURE 9. Average transverse momentum for π^+, K^+, p (left) and $\pi^-, K^-, \overline{p}$ as a function of the number of nucleons participating in the collision N_{part}.

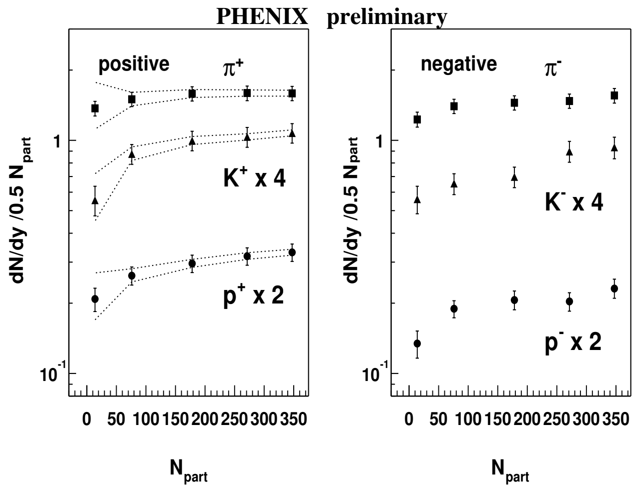

FIGURE 10. dN/dy per participant at mid-rapidity normalized to $|y| < 0.5$ for π^+, K^+, p (left) and $\pi^-, K^-, \overline{p}$ as a function of N_{part}. The error bars include statistical and systematic errors in dN/dy. The dashed lines around the π^+ points show the effect of the systematic error on N_{part} which affects all particles in the same way.

modification factor as the ratio,

$$R_{AA}(p_T) = \frac{(1/N_{evt})\, d^2N^{A+A}/dp_T d\eta}{(\langle N_{binary}\rangle/\sigma_{inel}^{N+N})\, d^2\sigma^{N+N}/dp_T d\eta}. \tag{3}$$

In the absence of nuclear modifications to hard scattering, the ratio R_{AA} will be unity; thus departures from $R_{AA} = 1$ indicate nuclear medium effects.

In this Section we examine high-p_T spectra of charged hadrons and neutral pions measured in a central and a peripheral class of collisions [36]. Charged particles are reconstructed using a drift chamber (DC) and two layers of multi-wire proportional chambers with pad-readout (PC1 and PC3) in the east arm. Neutral pions are measured in the central arms via their $\pi^0 \to \gamma\gamma$ decay. Two separate analyses are performed, the first using a lead-scintillator (PbSc) sampling calorimeter in half ($\Delta\phi = 45^o$) of the west arm aperture, and the second with a lead-glass Cerenkov (PbGl) calorimeter in a quarter ($\Delta\phi = 22.5^o$) of the east arm aperture (see Sections 2 and 5). The two analyses have very different systematics, and show the agreement of their final π^0 spectra.

The p_T distributions for charged hadrons and neutral pions are shown for two centrality classes in Fig. 11. The central sample covers the 0–10% most central fraction of the geometrical Au+Au cross-section, while the peripheral sample contains events in the 60–80% selection.

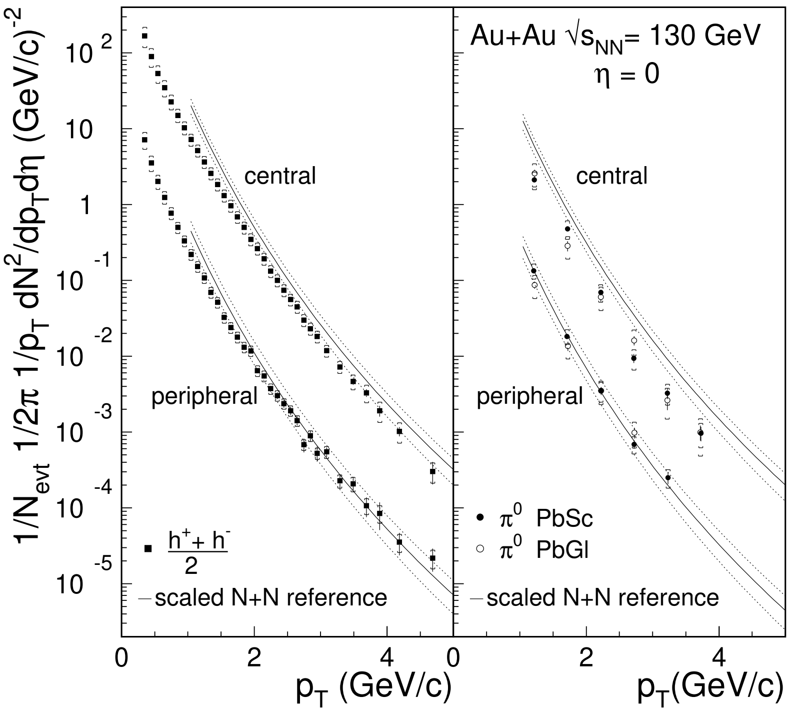

FIGURE 11. The yields per event at mid-rapidity for (*left*) charged hadrons and (*right*) neutral pions are shown as a function of p_T for 60–80% (*lower*) and 0–10% (*upper*) event samples, with the π^0 results from the PbSc and PbGl analyses plotted separately. The error bars indicate the statistical errors on the yield; the surrounding brackets indicate the systematic errors. Shown for reference are the yields per collision in N+N collisions, of charged hadrons and neutral pions respectively, each scaled up by $\langle N_{binary}\rangle$ for the class. The bands indicate both the uncertainty in the N+N reference and in the determination of $\langle N_{binary}\rangle$.

We estimate $\langle N_{binary}\rangle = 905 \pm 96$ for the central sample, $\langle N_{binary}\rangle = 20 \pm 6$ for the peripheral sample, and 45 ± 13 for the ratio between them. The data are compared to the binary-scaled yield from N+N collisions. We parameterize the cross section $1/(2\pi p_T)d^2\sigma/d\eta dp_T$ for N+N$\to$ $(h^+ + h^-)/2$ as $A/(1+p_T/p_0)^n$, with A =330 mb/GeV^2/c^2, p_0 =1.72 GeV/c, and n=12.4. Since no N+N data exist at $\sqrt{s}$ =130 GeV, we determine the parameters by interpolating between results for charged hadron production in p+p collisions at the ISR ($\sqrt{s}$ =23–63 GeV) [37] and in $\overline{\text{p}}$+p collisions from UA1 at CERN ($\sqrt{s}$ =200–900 GeV) [38] and CDF at FNAL ($\sqrt{s}$ =630,1800 GeV) [39]. To obtain a reference for neutral pions we presume $\pi^0 = (\pi^+ + \pi^-)/2$ and multiply the charge-averaged hadron cross section by the charged pion to charged hadron ratio π/h observed at the ISR [37]. This was found to be 0.63 ± 0.06 nearly independent of p_T above 1.5 GeV/c.

For $p_T > 2$ GeV/c the binary-scaling prediction agrees quite well with the data from peripheral collisions for both charged and neutrals. For central collisions, however, the data lie noticeably below the binary-scaling prediction for both spectra.

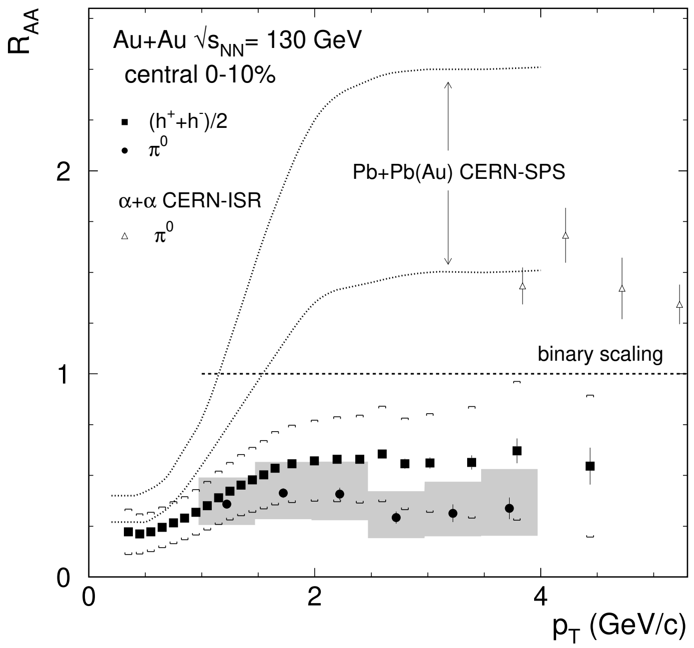

FIGURE 12. The ratio R_{AA} for charged hadrons and neutral pions (combined PbSc and PbGl results) in central Au+Au collisions. The error bars indicate the statistical errors on the measurement. The surrounding bands (shaded for π^0's, brackets for $(h^+ + h^-)/2$) are the quadrature sums of (i) the systematic errors on the measurement, (ii) the uncertainty in the p+p data, and (iii) the uncertainty in $\langle N_{binary} \rangle$. Also shown for reference are the ratio of inclusive cross sections in $\alpha + \alpha$ compared to p+p at $\sqrt{s_{NN}} = 31$ GeV (CERN-ISR) [42] and semi-inclusive spectra from central Pb+Pb, Pb+Au compared to p+p collisions at $\sqrt{s_{NN}} = 17$ GeV (CERN-SPS) [41] (shown as a band indicating the range of uncertainty covered by the errors on the CERN data).

To examine this difference more directly, we plot the ratio R_{AA} for central collisions in Fig. 12. Here and in Fig. 13 the π^0 spectra are a weighted average of the PbSc and PbGl results.

The depletion is quite striking, since the production of high-p_T hadrons in p+A collisions at fixed-target energies is known to be enhanced compared to the binary-scaling expectation for $p_T > 2$ GeV/c, ie the Cronin effect [35].

The ratio of yields from the two centrality classes, each divided by $\langle N_{binary} \rangle$, is plotted in Fig. 13. Many of the experimental uncertainties are reduced in this ratio. Like R_{AA} this ratio is below unity at all observed p_T for both charged hadrons and neutral pions, indicating a suppression of the yield per N+N collision in central collisions relative to peripheral.

The difference between the two ratios implies that the π/h ratio is smaller in central collisions than in peripheral (see discussion about π/p ratios in previous Section). The suppression of charged hadrons and neutral pions at high-p_T in central collisions is in qualitative agreement with the predictions of energy loss by scattered partons traversing a dense medium, like Quark Gluon Plasma, but other explanations cannot be ruled out at this time.

CONCLUSION

The PHENIX experiment has obtained results for Au + Au collisions at $\sqrt{s_{NN}} = 130$ GeV in the first physics run of RHIC. A hot dense nuclear medium is formed in these collisions. Many new interesting results were obtained, some of them are intrigueing, like (anti)proton aboundance and pion suppression at high-p_T. Many PHENIX results for radial flow, HBT interferometry, inclusive electron spectra are beyond this presentation. Much more is comming for $\sqrt{s_{NN}} = 200$ GeV in year-2001 run.

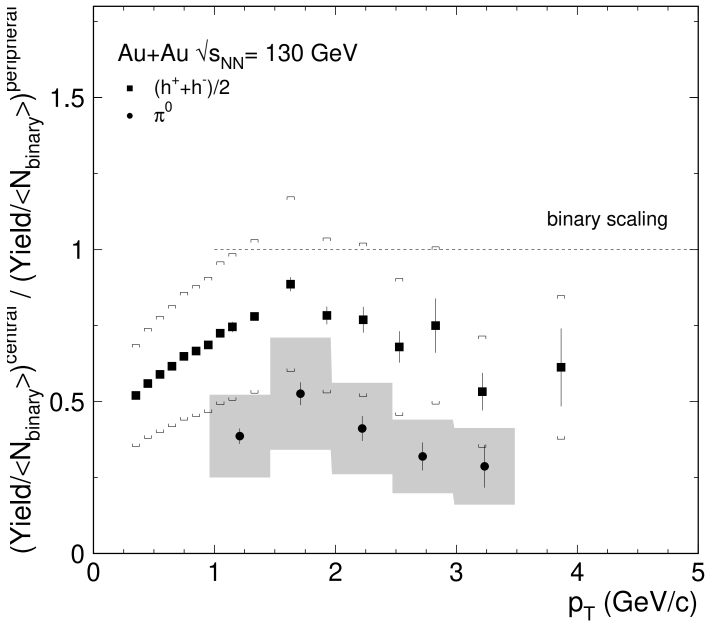

FIGURE 13. Ratio of yield per event in central *vs* peripheral Au+Au collisions, with each divided by $\langle N_{binary}\rangle$ for that class. The error bars indicate the statistical errors on the spectra. The surrounding bands (shaded for π^0's, brackets for $(h^+ + h^-)/2$) are the quadrature sums of (i) the parts of the systematic errors on the spectra that do not cancel in the ratio, and (ii) the uncertainty in $\langle N_{binary}\rangle$.

REFERENCES

1. PHENIX collaboration D.P.Morrison *et al.*, Nucl.Phys.**A638** (1998) 565c.
2. We used the Woods-Saxon nuclear density distribution, Au nucleus radius R=6.65±0.3fm, diffuseness a=0.54±0.01fm and nucleon-nucleon cross section σ_{nn}=40±5mb.
3. S.A. Bass *et al.*, Nucl. Phys. **A661**, 205c (1999).
4. X.N. Wang and M. Gyulassy, Phys. Rev. Lett. **86**, 3496 (2001) and nucl-th/0008014.
5. K.J. Eskola *et al.* Nucl. Phys. **B570**, 379 (2000) and hep-ph/0009246.
6. M.M. Aggarwal *et al.*, Eur. Phys. J. **C18**, 651 (2001) and nucl-ex/0008004.
7. F. Antinori *et al.*, Preprint CERN-EP-2000-002.
8. J. Bächler *et al.*, Nucl. Phys. **A661**, 45c (1999).
9. B.B. Back *et al.*, Phys. Rev. Lett. **85**, 3100 (2000).
10. PHENIX Collaboration, K.Adcox *et al.*,Phys.Rev.Lett.**86**, 3500 (2001).
11. PHENIX Collaboration, K.Adcox *et al.*,Phys.Rev.Lett.**87**, 052301-1 (2001).
12. J.D.Bjorken, Rhys.Rev.**D27**, 140 (1983).
13. NA49 Collaboration, T. Alber, *et al.*, Phys.Rev.Lett.**75**, 3814 (1995).
14. J.-Y. Ollitrault, Phys.Rev.**D46**, 229 (1992).
15. H. Sorge, Phys.Rev.Lett.**78**, 2309 (1997); *ibid.* **82**, 2048 (1999).
16. P. Danielewicz *et al.*, Phys.Rev.Lett.**81**, 2438 (1998).
17. C. Pinkenburg *et al.*, Phys.Rev.Lett.**83**, 1295 (1999).
18. D. Teaney, J. Lauret, and E.V. Shuryak, nucl-th/ 0011058.
19. P. F. Kolb *et al.*, hep-ph/0103234
20. R. Lacey *et al.*, Phys.Rev.Lett.**70**, 1224 (1993).
21. S. Wang *et al.*, Phys.Rev.C**44**, 1091 (1991).
22. D. Teaney, *et al.*, Phys.Rev.Lett.**86**,4783 (2001); nucl-th/0104041
23. P. Kolb, *et al.*, Phys.Lett. **B459**, 667(1999); nucl-th/0104041
24. J. Schaffner-Bielich, *et al.*, nucl-th/010848 and references therein
25. D. Kharzeev and M. Nardi, Phys.Lett. **B507**, 121 (2001);nucl-th/0108006

26. NA49 Collaboration, J. Bachler, *et al.*, Nucl.Phys. **A661**, 45 (1999).
27. NA44 Collaboration, I.G. Bearden, *et al.*, Phys.Rev.Lett **78**, 2080 (1997).
28. E866 Collaboration, L. Ahle, *et al.*, Nucl.Phys. **A638**,57 (1998)
29. P. Huovinen, *et al.* hep-ph/0101136
30. I. Vitev and Miklos Gyulassy. nucl-th/0104066
31. W. Broniowski and W. Florkowski. nucl-th/0106050
32. E735 Collaboration, T. Alexopoulos, *et el.*, Phys.Rev. **D48**, 984 (1993)
33. M. Gyulassy and M. Plümer, Phys.Lett. **B243**, 432 (1990); R. Baier *et al.*, Phys.Lett. **B345**, 277 (1995)
34. R. Baier, D. Schiff and B.G. Zakharov, Annu. Rev. Nucl. Part. Sci. **50**, 37 (2000).
35. D. Antreasyan *et al.*, Phys.Rev. **D19**, 764 (1979)
36. PHENIX Collaboration, K.Adcox *et al.*, nucl-ex/0109003
37. B. Alper *et al.*, Nucl.Phys. **B100**, 237 (1975)
38. C. Albajar *et al.*, Nucl.Phys. **B335**, 261 (1990)
39. F. Abe *et al.*, Phys.Rev.Lett. **61**, 1819 (1988)
40. X.N. Wang and M. Gyulassy, Phys.Rev.Lett. **68**, 1480 (1992); X.N. Wang, Phys.Rev. **C58**, 2321 (1998)
41. E. Wang & X.N. Wang, arXiv:nucl-th/0104031 and references therein
42. A.L.S. Angelis *et al.*, Phys.Lett. **B185**, 213 (1987)